Received 30 March 2018; accepted 5 May 2018. Date of publication 10 May 2018; date of current version 8 June 2018.
The review of this paper was arranged by Editor M. J. Kumar.

Digital Object Identifier 10.1109/JEDS.2018.2835153

Random Telegraph Signal Phenomena in Ultra Shallow p^+n Silicon Avalanche Diodes

VISHAL AGARWAL [1] (Student Member, IEEE), ANNE-JOHAN ANNEMA [1] (Member, IEEE), SATADAL DUTTA [2] (Student Member, IEEE), RAYMOND J. E. HUETING [2] (Senior Member, IEEE), LIS K. NANVER [2] (Life Member, IEEE), AND BRAM NAUTA [1] (Fellow, IEEE)

1 IC Design Group, Faculty of Electrical Engineering, Mathematics and Computer Science, University of Twente, 7500 AE Enschede, The Netherlands
2 MESA+ Institute for Nanotechnology, University of Twente, 7500 AE Enschede, The Netherlands

CORRESPONDING AUTHOR: V. AGARWAL (e-mail: v.agarwal@utwente.nl)

This work was supported by the NWO Domain Applied and Engineering Sciences, The Netherlands, under Project 12835.

ABSTRACT An extensive time domain analysis of the random telegraph signal (RTS) phenomena in silicon avalanche diodes is presented. Experiments show two distinct types of RTSs classified herein, on the basis of the temporal behavior of the amplitude, as the "decaying" and the "constant" type. These RTSs are analyzed using a model for defects reported earlier, from which their ohmic series resistance and geometrical parameters have been estimated. The results indicate that breakdown of a relatively small area defect results in a "decaying" amplitude type of RTS, and breakdown of a relatively large area defect results in a "constant" amplitude type of RTS. These two types can be explained by the differences in the thermal resistance, which is higher for the former.

INDEX TERMS Avalanche breakdown, avalanche diodes, microplasma, random telegraph noise, random telegraph signal, time domain analysis.

I. INTRODUCTION

Deterministic and statistical carrier multiplication theories have been reported in literature to describe the triggering of avalanche in Silicon (Si) diodes in [1]–[4] (and in references therein). In applications like optical detectors based on avalanche photodiodes (APDs) [5] or single-photon avalanche diodes (SPADs) [6], the avalanche phenomenon is utilized to detect weak optical signals. Moreover, during avalanche, Si diodes emit light at visible wavelengths, which is attractive for monolithic integration of optical links in CMOS technologies because of strong overlap of their emission spectrum with the responsivity of standard Si detectors [7]–[10].

Random Telegraph Signal (RTS) phenomena in the avalanche current at the onset of breakdown were reported earlier [11], [12]. Initially, the RTS phenomena were referred to as the "microplasma instability" because during breakdown, it was shown that these unstable localized defects emitted visible light [13]. Many interesting theories were presented to provide a phenomenological description of these current fluctuations [14]–[17]. It was established that these fluctuations arise from crystal defects such as dislocations in the diodes [16]. The concept of RTS phenomena to model these fluctuations was discussed in [14]. Recently, the modeling has been revisited [3]. An elaborate overview of the evolution of this topic has also been presented in the same paper [3].

In [18], we reported that the avalanche process and its current-voltage ($I-V$) characteristics can be described by RTS phenomena. From the RTS analysis results, we could model the $I-V$ characteristics. The impact of the RTS analysis on the accurate design of quenching and recharge circuits for SPADs is also discussed in [18]. That work can be used to increase the count rates and to decrease the afterpulsing in SPADs. Further, the non-monotonic behavior of the noise spectral density in reverse biased diodes is caused by RTS phenomena [19]. As discussed in [3] and [20], studying RTS phenomena is also useful for determining the material quality and for reliability analyses of, e.g., power devices, because RTS phenomena are caused by crystal defects.

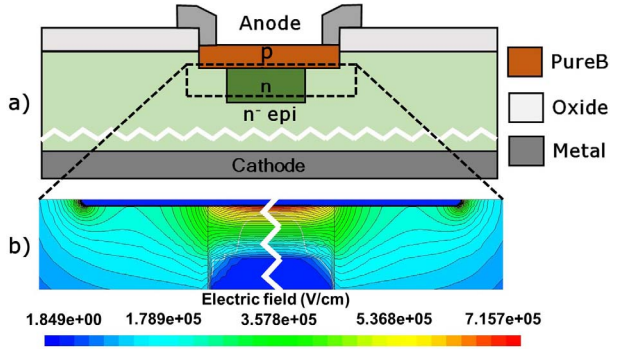

FIGURE 1. **(a) Schematic cross-section of a circular p^+n diode in PureB technology. The diameter is defined by the dimensions of the n layer. (b) TCAD simulated electric field of the highlighted region above breakdown (15 V) showing a lateral uniform field in the depletion region.**

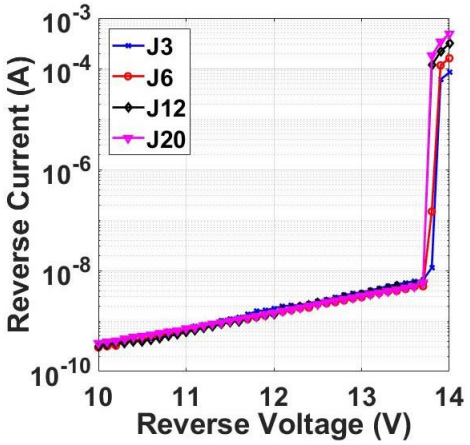

FIGURE 2. **Measured reverse biased *I-V* characteristics of all diodes at 25 °C.**

Time domain analysis (TDA) of the RTS phenomena can be used to estimate the properties of defects causing these RTSs. The TDA methods and the experimental setup to characterize RTSs were developed after the 1960s. Possibly because of experimental limitations, an extensive TDA of RTS phenomena in avalanche diodes is missing in the literature. The purpose of this work is to address this issue. The main findings of this paper are:

- From the temporal behavior of the RTS amplitude, it is shown that two types of defects with different local thermal impedances exist in diodes. Defects with a high thermal impedance cause a "decaying" type of amplitude in RTSs and defects with a low thermal impedance cause a "constant" type of amplitude in RTSs.
- Using the TDA, it is shown that the bumpy behavior in the current-voltage characteristics is caused by the two types of defects and not necessarily by the relatively high thermal impedance of the diode packaging as reported earlier [16].
- An existing model for these defects is improved to take into account an explicit thermal model. Using the model, both the ohmic series resistance and the dimensions of these defects are estimated.

The paper is outlined as follows: the experimental diodes and measurement setup to measure the RTS phenomena are described in Section II. The analysis method for the two types of RTSs is discussed in Section III. In Section IV, we show the geometry dependency of various RTS parameters. A model for the defects causing these RTS phenomena is used for estimating some of the electrical and geometrical parameters of the defects in Section V. Finally, in Section VI we summarize the main findings of this work.

II. EXPERIMENTAL SETUP

A. EXPERIMENTAL DIODES

In this work, we aim at avalanche processes in devices used for optical generation and detection, requiring semiconductor-only junctions. Therefore, for our experiments, we adopted diodes designed in a pure boron (PureB) technology [21]. In this technology, a thin layer of PureB is deposited by chemical vapor deposition on a clean n-Si surface. P-type Si is obtained from this thin PureB layer and high quality ultra-shallow p^+-n, hence abrupt asymmetric, junctions are obtained [22]. These ultra-shallow junctions are suitable for various optical detection or emission applications [21]–[23]. Four circular diodes, on the same die, were selected with diameters of 3 μm, 6 μm, 12 μm and 20 μm; we label these diodes as J3, J6, J12 and J20 respectively, where the diode name indicates its diameter. A TCAD simulated electric field of a representative device at breakdown showing a uniform lateral field in the depletion region is shown in Fig. 1(b). Due to the circular geometry, the lateral electric field in the depletion region should be uniform at breakdown. However, the electric field is distorted at crystal defects, forming the preferred location of breakdown [16].

Fig. 2 shows DC *I-V* characteristics of all diodes at 25 °C in dark conditions measured by an Agilent B2901A Source/Measure Unit (SMU) using 1 s integration time. In these diodes, the avalanche starts at around 13.7 V; the reverse current (I_R) rises sharply between the reverse voltage (V_R) of 13.7 and 13.9 V. This work focuses on this voltage range.

B. MEASUREMENT SETUP AND ANALYSIS METHOD

The measurement setup and the TDA method have been described extensively in [18]. The relevant details are briefly summarized here.

Fig. 3(a) shows the experimental setup to measure the RTS phenomena. The cathode is biased at a constant voltage and the RTSs were measured across a 50 Ω resistance, thus providing a low impedance load and a low quenching. A low noise SIM 911 preamplifier was used to drive the oscilloscope input to improve the signal-to-noise ratio at the oscilloscope input. The transient data were acquired for a total duration of 1 s at each reverse bias voltage for all

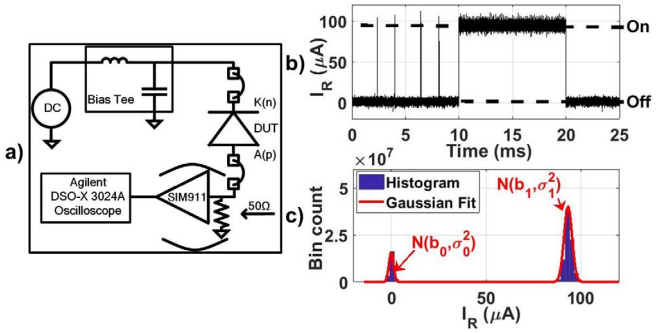

FIGURE 3. (a) RTS measurement setup. (b) Example of measured RTSs in I_R. (c) Histogram of the measured RTSs.

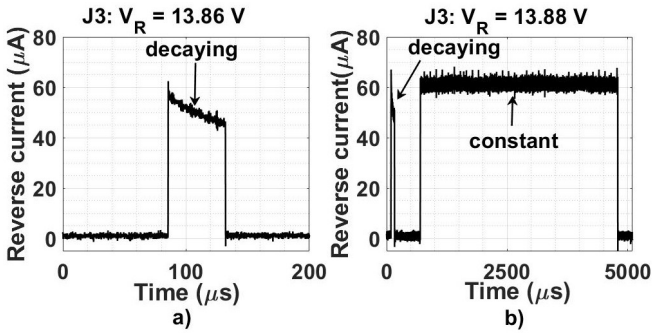

FIGURE 4. (a) A "decaying" type of RTS observed at a lower V_R. (b) Mixture of a "constant" and a "decaying" RTS at a higher V_R in the same diode. The x-axis scales are different for clarity.

diodes, at a data acquisition rate of 100 MS/s. The measurements were done in a Faraday cage in dark condition using wafer probing.

Fig. 3(b) shows an example of the measured I_R in the steep part of the $I-V$ characteristics, showing the RTS phenomena in the I_R of these diodes. This I_R can be represented in a histogram as shown in Fig. 3(c). A sum of two Gaussians, $N(b_0, \sigma_0^2)$ and $N(b_1, \sigma_1^2)$, is fitted on this histogram and from the fit parameters, the mean value of the off-state (b_0) and the mean value of the on-state (b_1) are estimated. The RTS amplitude (ΔI_{RTS}) is obtained from these fit parameters. Also, from the mean on-time ($E(T_{ON})$) and mean off-time ($E(T_{OFF})$), the mean on-time fraction ($E(D)$) can be estimated, the detailed procedure has been described in [18]. The mathematical equations for the estimation of relevant parameters are summarized in Eq. (1):

$$\Delta I_{RTS} = b_1 - b_0, \tag{1a}$$

$$E(D) = \frac{E(T_{ON})}{E(T_{ON}) + E(T_{OFF})}. \tag{1b}$$

$E(D)$ represents the fraction of time, in an observed time window, where the RTS is in the on-state (Fig. 3(b)). Note that two types of RTSs are observed in these diodes (see Section III). In the definitions of $E(D)$ and ΔI_{RTS}, we do not distinguish between these two types of RTSs.

III. RTS CHARACTERIZATION

We have observed two types of RTSs in our diodes. For example, for J3, at a relatively low V_R (at the onset of breakdown), the RTSs were decaying in amplitude during RTS events as shown in Fig. 4(a). We denote this as the "decaying" amplitude type of RTS. At a higher V_R (slightly above the breakdown voltage), another type of RTS with a constant amplitude, denoted as the "constant" amplitude type was also observed, as shown in Fig. 4(b). To our best knowledge, a mixture of "decaying" and "constant" types of RTSs at a given bias in a single diode has not been reported before.

A possible explanation for the two types of the RTSs was provided in [16]. It was predicted that the "decaying" RTSs will be observed in diodes which are not in a good thermal contact with the outside world. For such diodes, the energy dissipated during the avalanche process would increase the temperature of the diode. This decreases the effective impact ionization coefficient (α) and consequently decreases the avalanche current [24]. Interestingly, it was assumed that the local thermal impedance of a defect inside the diode is negligible [16]. The above explanation implies that a mixture of defects with different local thermal impedances in a single device is not possible, contrary to our observations. Assuming thermal effects as the root cause for the different RTSs would imply that there are at least two different defects in the same diode: one with a relatively low and the other with a relatively high thermal impedance with the outside world.

A. RTS CLASSIFICATION

The measured transient data were analyzed in MATLAB. From the transient data acquired for 1 s, all individual RTSs were identified and many RTS properties were extracted. These properties are the peak current (I_{peak}), pulse width (PW), the decay time constant for the "decaying" RTSs (τ, see Section V) and the shape of the RTS.

To distinguish between the "decaying" and the "constant" types of RTS, the decay in the RTS amplitude during each pulse was estimated. Firstly, the PW of each RTS was extracted from its rising and falling edges. For estimating the time constant (τ), the RTS current $I_R(t)$ was fitted onto an exponentially decaying transient current model (Fig. 5):

$$I_R(t) = I_0 \cdot e^{-t/\tau}, \tag{2}$$

where τ is a fitting parameter. Based on the ratio of PW/τ, the decay in the RTS amplitude was calculated. For a decay of less than 1% during the PW, the shape of the RTS was labeled as a "constant" amplitude type.

$$\text{RTS type} = \begin{cases} \text{constant amplitude}, & \text{if } \frac{PW}{\tau} \leq 0.01 \\ \text{decaying amplitude} & \text{otherwise.} \end{cases} \tag{3}$$

Fig. 5 shows an example of a measured and its fitted pulse for both types of RTSs.

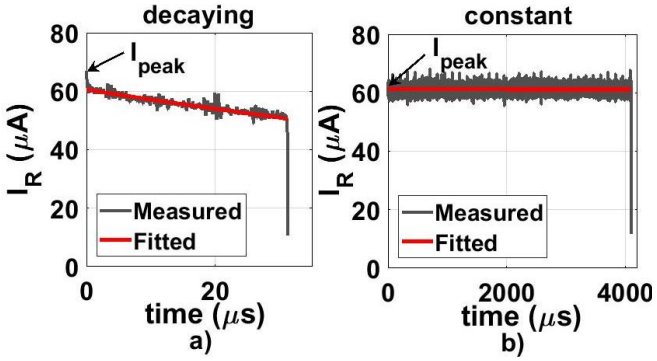

FIGURE 5. Classifying the RTS: (a) A "decaying" RTS : $PW = 31.47\ \mu s$, $\tau = 183.9\ \mu s$, and a decay of $\sim 16\%$. (b) A "constant" RTS : $PW = 4.09 \times 10^3\ \mu s$, $\tau = 3.3 \times 10^6\ \mu s$. The peak current ($I_{peak}$) was separately extracted.

The peak current (I_{peak}, see Fig. 5) of each RTS was also separately extracted. The I_{peak} is used in Section V to estimate the parameters of the defects.

B. FRACTION OF "CONSTANT" RTSs

Fig. 6 shows the fraction of "constant" type of RTSs ($F(V_R)$) as a function of V_R for all diodes:

$$F(V_R) = \frac{N_{constant}(V_R)}{N_{constant}(V_R) + N_{decaying}(V_R)}, \quad (4)$$

where $N_{constant}(V_R)$ and $N_{decaying}(V_R)$ are the number of "constant" and "decaying" types of RTSs per unit time respectively, observed at each V_R. From the $F-V$ curve, we can estimate the V_R at which the "constant" type of RTSs start appearing, i.e., $F > 0$. At a few bias points, $0 < F < 1$, both types of RTSs were observed.

Fig. 6 shows that the "constant" type of RTSs appear for higher V_R than the "decaying" type of RTSs. As discussed in Section IV, the V_R at which F starts to sharply increase is the V_R at which a bump in the RTS parameters, ΔI_{RTS} and $E(D)$, were observed.

C. MEAN PULSE WIDTH

Fig. 7 shows the mean pulse width (PW_{MEAN}) of the "constant" and the "decaying" RTSs as a function of V_R. The mean values were obtained from all observed RTSs for each type at each bias condition. The "decaying" RTSs have a lower PW_{MEAN} compared to the "constant" RTSs. This can be explained by the local heating providing negative feedback for the avalanche process by reducing the excess bias across the diode (Section V), thereby reducing α. The avalanche at such a "hotspot" quenches relatively quickly because of decreasing α [24]. Further, the PW_{MEAN} increases with V_R because of the increasing electric field, which helps to sustain the avalanche for a longer time. The "constant" amplitude RTSs have a much larger PW_{MEAN}, possibly due to the absence of significant thermal effects. For "constant" RTSs, the accuracy of the estimated PW_{MEAN} reduces for higher V_R because of fewer events in 1 s measurement time.

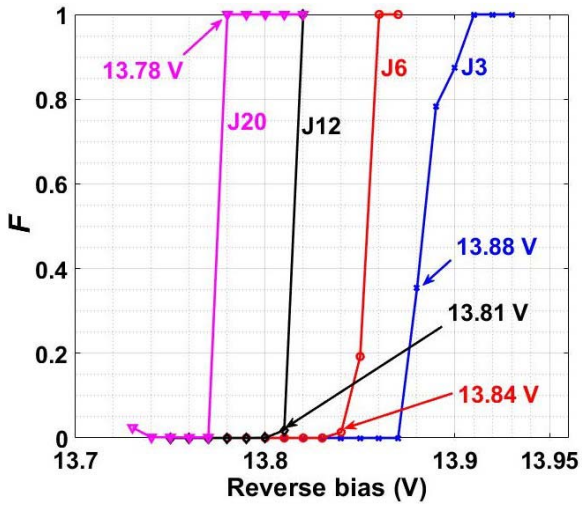

FIGURE 6. Fraction of "constant" amplitude RTSs (F) as a function of V_R (Eq. 4).

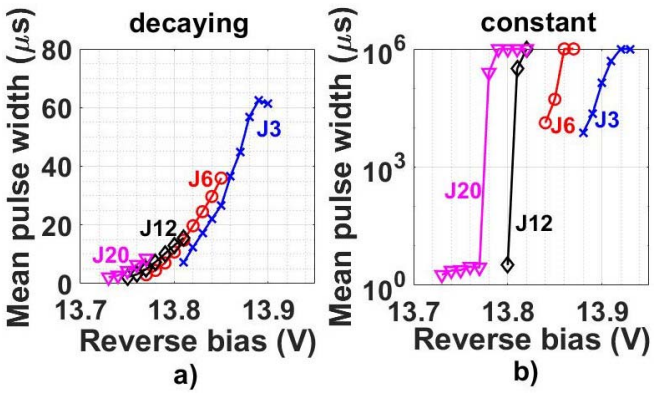

FIGURE 7. Mean pulse width (PW_{MEAN}) as a function of V_R for (a) "decaying" (b) "constant" amplitude RTSs. Y-axis are different for clarity. A PW_{MEAN} of 1 s implies that no RTSs were observed at that bias setting and the diode was in a continuous On-state.

However, the measured accuracy is sufficient for our purpose of modeling and estimation of the defect parameters.

IV. BIAS DEPENDENT RTS PARAMETERS

The statistical properties of the RTSs, namely ΔI_{RTS} and $E(D)$ were obtained as a function of V_R for all diodes. The arrival times between the RTS pulses, also referred to as inter-arrival times, have been shown to be exponentially distributed [16], [18], [25], which confirms that the observed RTS process has a Poisson distribution.

A. RTS AMPLITUDE

Fig. 8 shows that ΔI_{RTS} increases with V_R. The bump in the $\Delta I_{RTS} - V$ characteristics at the indicated V_R (Fig. 8) is also important to note. Such a bump was believed to be caused by the relatively high thermal impedance of the diode with the outside world [16]. It was thought that if the diode is not in a good thermal contact with its heat sink, such $\Delta I_{RTS} - V$ characteristics would be obtained. However,

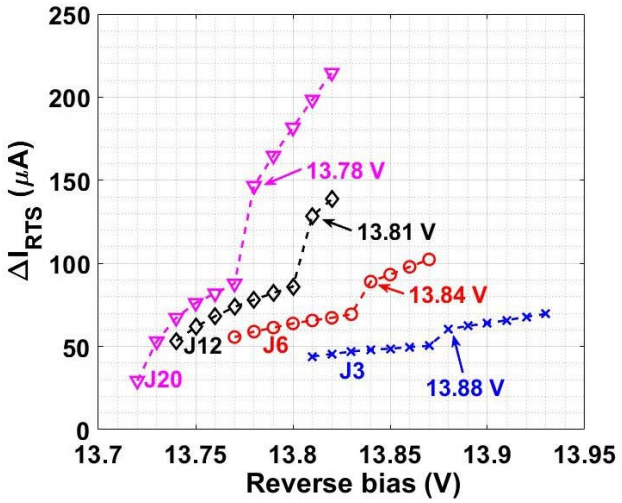

FIGURE 8. RTS amplitude (ΔI_{RTS}) as a function of V_R. At the indicated V_R, "constant" amplitude RTSs are triggered (Fig. 6).

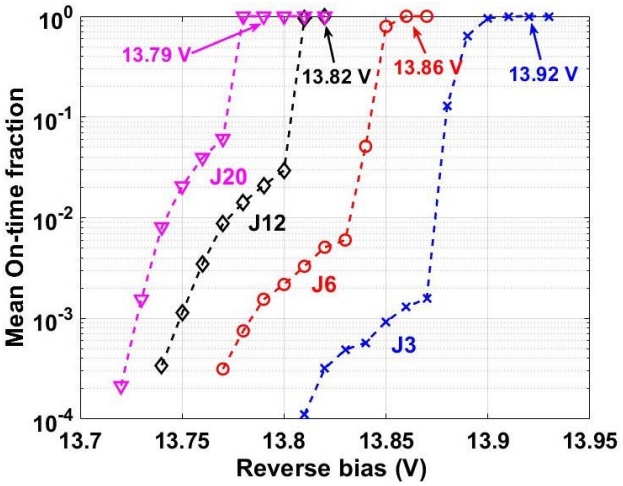

FIGURE 9. Mean ON-time fraction ($E(D)$) as a function of V_R. At and above the indicated V_R, $E(D) = 1$; the diodes were in a continuously On-state above these V_R.

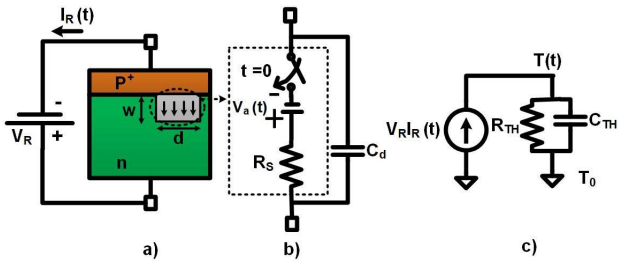

FIGURE 10. (a) Schematic cross-section of a cylindrical defect of height w and diameter d inside a p$^+$-n junction. (b) Circuit model for the defect comprising of avalanche sustaining voltage V_a, series resistance R_S, bistable switch and diode capacitance C_d. (c) A thermal model to estimate the temperature of the defect region.

as shown in Section III, at and above these V_R, defects causing the "constant" amplitude RTSs are triggered; the bumpy behavior is a result of those RTSs.

B. MEAN ON-TIME FRACTION

Fig. 9 shows $E(D)$ (Eq. (1b)) as a function of V_R. The $E(D)$ sharply increases as a function of V_R close to breakdown. As explained in [18], the steep $I-V$ dependency in avalanche is mainly because of this steep dependency of $E(D)$ on V_R. The bump at a higher V_R is due to the onset of the "constant" amplitude type of RTSs at higher V_R which have higher PW_{MEAN}, as discussed in Section III. As the size increases (from J3 towards J20), the V_R range over which the RTS phenomena are observed (the range in which $0 < E(D) < 1$) decreases. This can be attributed to an increasing number of crystal defects with increasing size of the diode [26].

The $\Delta I_{RTS} - V$ and $E(D) - V$ characteristics are used to estimate a few properties of defects in Section V.

V. ESTIMATION OF MODEL PARAMETERS

In this section, we estimate the electrical and geometrical parameters of the defects causing the RTS phenomena, based on the model from [16]. First, we discuss the model and its relevant characteristics. Then, we estimate the electrical parameters of the defects using TDA results. From the electrial parameters, geometrical details of the defects causing the two types of RTSs are estimated.

Fig. 10(a) shows the schematic cross-section of a defect causing these RTS phenomena. For simplicity, a defect is modeled as a cylinder of height w and diameter d and avalanche is assumed to be confined in this cylinder [16]. As reported earlier, w is the depletion layer width [3], [16].

Fig. 10(b) shows the circuit model of the defect. The bistable switch models the on-off switching characteristics of the defect causing the RTS phenomenon. The charge fluctuations in the defect region control this switch [3]. The $V_a(t)$ in the model corresponds to the voltage at which the multiplication factor (M) is unity [16]. Once the avalanche is triggered, the free carriers partially neutralize the space charge and thereby reduce the electric field. Then, the applied V_R should be increased to keep I_R constant; the resistance produced by this partial neutralization of space charge because of high injection in the defect region is denoted as the space charge resistance (R_S) (Section V-C) [15], [16], [24], [27], [28].

Once the avalanche is triggered, the temperature of the defect region $T(t)$ starts to increase because of the energy dissipated during the avalanche process. This rise in temperature is modeled by a thermal model incorporating a thermal resistance and thermal capacitance, R_{TH} and C_{TH} respectively [29], as shown in Fig. 10(c).

With Fig. 10(b), the RTS current $I_R(t)$ is:

$$I_R(t) = \frac{V_R - V_a(t)}{R_S}. \tag{5}$$

An elevated $T(t)$ results in an increased $V_a(t)$ [16], thereby providing a negative feedback for the avalanche process. In our devices, the doping $N_D \sim 10^{17}$ [cm^{-3}], and for such N_D, the V_a can be approximated with a linear dependence

on $T(t)$ [30], [31]:

$$V_a(t) = V_{a0} + \beta \cdot (T(t) - T_0), \tag{6}$$

where β ($\sim$ 5 mV/K) is the thermal coefficient for the breakdown voltage [31], T_0 is the initial temperature at $t = 0$ and V_{a0} is V_a at $T = T_0$. The $T(t)$ due to self heating is:

$$T(t) = T_f - (T_f - T_0) \cdot e^{-t/\tau}, \tag{7a}$$

$$T_f \approx T_0 + \frac{R_{TH} V_R (V_R + \beta T_0 - V_{a0})}{R_S + \beta R_{TH} V_R}, \tag{7b}$$

$$\tau = \frac{R_{TH} R_S C_{TH}}{R_S + \beta R_{TH} V_R}. \tag{7c}$$

The physical variables in the above equations are:

- T_f is the temperature in thermal equilibrium at $t \to \infty$ assuming that the avalanche is not quenched.
- R_{TH} ([K/W]) is the thermal resistance of the avalanche region.
- C_{TH} ([Ws/K]) is the thermal capacitance of the avalanche region.

An expression for $R_{TH} = (T_f - T_0)/(V_R I_R)$ has been derived in [16]:

$$R_{TH} = \frac{1}{\pi k d \left(\frac{w}{d}\right)} \left(\frac{w}{4d} \sqrt{1 + \left(\frac{w}{d}\right)^2} + \frac{1}{8} \ln \left(\frac{\sqrt{1 + (\frac{w}{d})^2} + \frac{w}{d}}{\sqrt{1 + (\frac{w}{d})^2} - \frac{w}{d}} \right) \right), \tag{8}$$

where k ($\sim$ 2 W/cm-K) is the thermal conductivity of Si [28]. In our devices, for typical values of w and d (Section V-C), $\beta R_{TH} V_R$ is much smaller than R_S, therefore $\tau \approx R_{TH} C_{TH}$ (Eq. (7c)).

Using Eqs. (5)–(7), $I_R(t)$ can be written as:

$$I_R(t) = \frac{V_R - V_{a0}}{R_S} - \frac{\beta \cdot (T_f - T_0)}{R_S} \cdot \left(1 - e^{-t/\tau}\right). \tag{9}$$

The peak current (I_{peak}) of this $I_R(t)$ is given by:

$$I_{peak} = I_R(t = 0) = \frac{V_R - V_{a0}}{R_S} = \frac{V_{EX}}{R_S}. \tag{10}$$

It is important to note that I_{peak} is dependent only on the initial excess bias ($V_{EX} = V_R - V_{a0}$) and R_S. From the slope of the measured $I_{peak} - V_{EX}$ characteristics, the R_S can be estimated:

$$\frac{1}{R_S} = \frac{dI_{peak}}{dV_R} = \frac{dI_{peak}}{dV_{EX}}. \tag{11}$$

Further, from the estimated R_S, the effective d of the defects are estimated in Section V-C.

Eq. (9) indicates that $I_R(t)$ decays with a time constant $\tau \approx R_{TH} C_{TH}$. The decay time constant of $I_R(t)$ has been estimated in Section III; the results are shown here for completeness of the model.

In this section, we model two lumped defects in one diode: one causing the "decaying" amplitude RTSs and the other causing the "constant" amplitude RTSs. Multiple defects with similar breakdown voltage and resistance cannot be distinguished using TDA.

a)

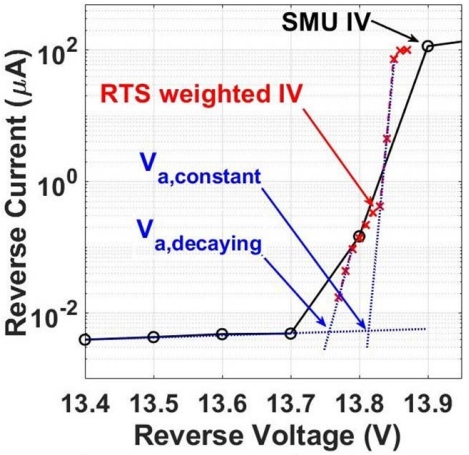

b)

Diode	$V_{a,decaying}$ (V)	$V_{a,constant}$ (V)
J3	13.81	13.87
J6	13.75	13.81
J12	13.73	13.80
J20	13.72	13.76

FIGURE 11. Estimation of V_{a0} for J6. (a) The intersection of SMU $I - V$ and RTS weighted $E(D) \cdot \Delta I_{RTS} - V$ characteristics is the voltage at which $M = 2$. From the intersection of two types of curves, the V_{a0} for the defects causing "decaying" ($V_{a,decaying}$) and "constant" amplitude RTSs ($V_{a,constant}$) are estimated. (b) Summary of $V_{a,decaying}$ and $V_{a,constant}$ for all diodes.

A. ESTIMATING V_{a0}

As mentioned before, V_{a0} is defined as the voltage at which $M = 1$ at $T = T_0$ [16]. However, estimating this voltage is by no means straight forward. In [18], we have proposed an alternative definition of the experimental breakdown voltage (V_{BR}) being the voltage at which $M = 2$. This is estimated from the SMU measured $I - V$ characteristics and the RTS weighted $E(D) \cdot \Delta I_{RTS} - V$ characteristics. The term $E(D) \cdot \Delta I_{RTS}$ represents the average current of the RTS current pulses. The current during the on-state of the RTSs is due to impact ionization.

Both the SMU measured $I - V$ and the RTS weighted $E(D) \cdot \Delta I_{RTS} - V$ curves were extrapolated (dashed lines in Fig. 11(a)). The intersection of these extrapolated curves is the voltage at which the RTS weighted current contribution equals the leakage current component, hence $M = 2$. This voltage is denoted as $V_{M=2}$ and will be used as approximation for V_{a0}. In reality, V_{a0} would be somewhat lower than $V_{M=2}$.

There are two different types of defects in our diodes causing two types of RTSs and the V_{a0} is different for both defects. Fig. 11(a) shows the example procedure for estimating V_{a0} for both types of defects in J6, i.e., $V_{a,decaying}$ and $V_{a,constant}$; a similar procedure was carried out for other

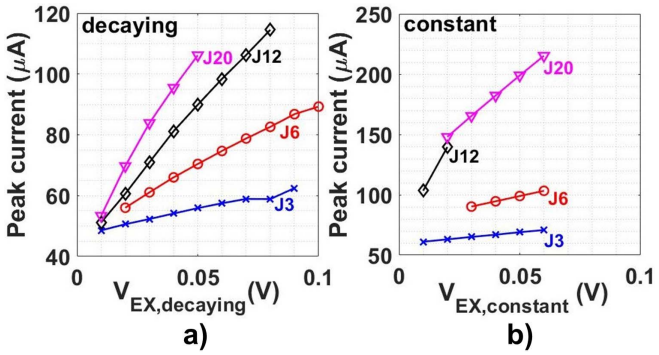

FIGURE 12. Mean peak current (I_{peak}) of various diodes as a function of V_{EX}: (a) for the "decaying" amplitude RTSs. (b) for the "constant" amplitude RTSs. The y-axis scales are different for clarity.

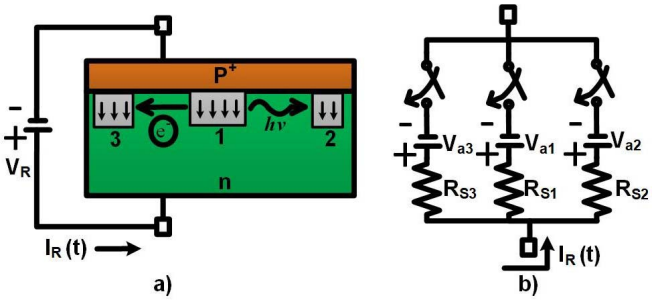

FIGURE 13. a) Illustration of spreading of avalanche where multiple defects in a single diode are involved. First defect 1 is triggered, then defect 2 is triggered by secondary photons emitted by defect 1 and defect 3 by lateral transport of free carriers. b) Equivalent circuit model for modeling the spreading effect for three defects.

diodes and the results are summarized in Fig. 11(b). The "constant" amplitude RTSs have a higher $V_{a,constant}$. These voltages are used in estimating V_{EX} to calculate R_S.

B. PEAK CURRENT

Fig. 12 shows the mean value of measured I_{peak} (Fig. 5) as a function of $V_{EX}(= V_R - V_{a0})$ of all diodes and for both types of RTSs. The mean values were estimated using all observed RTSs of each type at all bias conditions. It is observed that I_{peak} increases with V_{EX}.

The offset in I_{peak} around $V_{EX} = 0$ is most likely because the actual V_{a0} is lower than $V_{M=2}$. In the measurement duration of 1 s (Section II), no RTS phenomenon was observed at $V_R < V_{a0}$.

The RTSs are caused by localized defects inside the devices [3], [14], [16]. The observed increase in I_{peak} for larger diodes is most likely due to the spreading of avalanche to secondary defects, once a single defect is triggered. As the size of the diode increases, the number of defects causing RTS phenomena increases (see also Appendix B). This could cause the avalanche triggered at a defect site to trigger secondary defects by two mechanisms [32]: 1) drift and diffusion of free carriers in lateral direction and 2) emission of secondary photons. As reported in [32], this spreading of avalanche occurs in a few tens of picoseconds. Fig. 13(a) illustrates this process.

Hence, the measured I_{peak} could originate from breakdown at multiple defects (Fig. 13(b)):

$$I_{peak} = \sum_{i=1}^{n} \frac{V_R - V_{a,i}}{R_{S,i}} \tag{12}$$

where $V_{a,i}$ and $R_{S,i}$ are the breakdown voltage and the series resistance of the ith defect.

C. SERIES RESISTANCE AND GEOMETRICAL DETAILS OF THE DEFECTS

As stated before, the resistance due to the partial neutralization of space charge in the avalanche region is referred to as the space-charge resistance (R_S). Using Eq. (11) and Fig. 12, R_S was estimated for the two types of defects for all diodes. An example of the procedure for estimating R_S is shown in Fig. 14(a). The estimated R_S of defects in all diodes are shown in Fig. 14(b). The results indicate that the defects causing "decaying" amplitude RTSs have a higher R_S than the defects causing "constant" amplitude RTSs. The relatively low R_S for larger diodes can also be explained by a simultaneous breakdown of multiple defects (Fig. 13):

$$\frac{1}{R_S} = \sum_{i=1}^{n} \frac{1}{R_{S,i}}. \tag{13}$$

Alternatively, each component in R_S can be described by the dimensions of a single defect and the properties of the diode (impurity concentration). For a defect inside a single sided abrupt p$^+$−n junction, its $R_{S,i}$ is given by [28]:

$$R_{S,i} = \frac{2\,(w - x_A)^2}{\pi\,\varepsilon_S v_S {d_i}^2} \tag{14}$$

where w is the depletion region width, x_A is the avalanche region width where most of the multiplication takes place [28], $\varepsilon_s = 1.04 \times 10^{-12}$ F/cm^2 is the permittivity of Si, $v_s = 1 \times 10^7$ cm/s is the saturation velocity of electrons and holes and d_i is the diameter of the ith defect. For simplicity, v_s is assumed the same for electrons and holes [3], [28]. For single-sided abrupt junctions: $x_A \sim 0.3w$ [3].

From the estimated R_S, the value of the effective diameter d is estimated and results are tabulated in Fig. 14(c) for both types of defects for all devices. According to Eqs. (13) and (14), d is an effective value possibly obtained from the breakdown of many defects:

$$d = \sqrt{\sum_{i=1}^{n} {d_i}^2}, \tag{15}$$

where d_i is the diameter of the ith defect. The first observation from Fig. 14(c) is that the defects causing "decaying" amplitude RTSs have a relatively smaller d than the defects causing "constant" amplitude ones. The second observation is the increasing effective size of the defects with the size of the device as discussed and explained by the

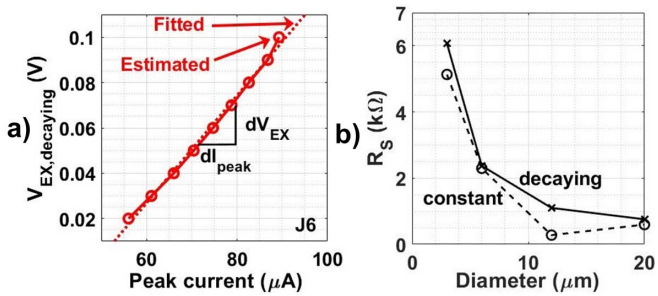

c)

Device	J3	J6	J12	J20
decaying d (μm)	0.97	1.56	2.29	2.76
constant d (μm)	1.06	1.59	4.57	3.11

FIGURE 14. **a) Example procedure for estimating $R_S = dV_{EX}/dI_{peak}$ for "decaying" amplitude RTSs in J6. b) Estimated R_S of the defects causing "decaying" and "constant" amplitude RTSs. c) Estimated diameter d for both types of defects in all diodes. The d for defect causing "constant" amplitude RTSs in J12 is larger than that in J20. This is also observed from optical measurements (Appendix C).**

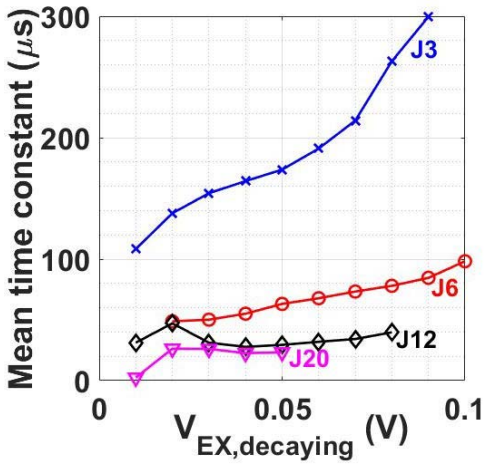

FIGURE 15. **Mean thermal time constant (τ) of "decaying" amplitude RTSs as a function of $V_{EX,decaying}$.**

spreading of avalanche to multiple defects in large diodes. The estimated d is in the same order of magnitude as the reported values in the literature obtained from optical measurements [3], [16], [17]. Also, our optical measurements confirmed this (Appendix C).

D. THERMAL TIME CONSTANT

Fig. 15 shows the estimated thermal time constant ($\tau \approx R_{TH}C_{TH}$) of the "decaying" amplitude RTSs (Section III). The figure shows that τ increases with increasing $V_{EX,decaying}$.

It was observed using the light emission properties of the defects that the d remains almost constant over the instability region [16]. The w increases with increasing $V_{EX,decaying}$ and therefore the R_{TH} should increase with increasing w/d (Eq. 8), also predicted in [16]. Also, C_{TH} increases proportionally with the volume of the defect [33]. This complies with the observed increasing behavior of τ with $V_{EX,decaying}$. At a given V_{EX}, τ decreases for larger diodes because of larger d (Section V-C).

VI. CONCLUSION

We presented an extensive time domain analysis of RTS phenomena in the diode current in avalanche. Using the analysis results, we showed the dependency of RTS parameters (amplitude and mean on-time fraction) on the size of the diode. The amplitude of the RTSs was shown to increase with the area of the diode which was explained by the spreading of avalanche to more defects in larger diodes. The steep DC measured $I-V$ dependency close to breakdown was shown to be due to the steep dependency of on-time fraction of RTSs on bias voltage. Two different types of RTSs were observed in these diodes: a "decaying" and a "constant" amplitude type and a comprehensive analysis of both RTSs was done. It was proposed that the "decaying" amplitude RTSs are caused by defects having relatively high thermal impedance. We adopted a model for the defects causing these RTS phenomena from the literature, and some of the defect parameters were estimated using the time domain analysis. The ohmic series resistances of these defects were estimated to be hundreds of ohms to a few kΩ. The diameter of the defects was estimated to be in the order of a few μm. Further, it was argued that the "decaying" amplitude RTSs are caused by relatively small area defects and the "constant" amplitude RTSs by relatively large area defects. The demonstrated analysis procedure for estimating a defect's series resistance and its dimensions can be readily used in other devices as well.

APPENDIX A
MULTIPLICATION NOISE IN ON-STATE

The multiplication noise during avalanche (σ_M) can also be estimated from the measured RTSs. Firstly, the transient noise in the On-state of an RTS ($I_n(t)$) was estimated from the measured ($I_{Meas}(t)$) and the fitted data ($I_R(t)$, see Eq. (2)):

$$I_n(t) = I_{Meas}(t) - I_R(t). \tag{16}$$

Fig. 16(a) illustrates an example of the procedure of estimating $I_n(t)$ for "decaying" amplitude RTSs. A similar procedure was used for "constant" amplitude RTSs. At a given bias, $I_n(t)$ was estimated for each RTS of either type. These $I_n(t)'s$ were represented as a histogram. An example of the histogram obtained for the "decaying" amplitude RTSs is shown in Fig. 16(b). A Gaussian ($N(b_n, {\sigma_n}^2)$) was fitted on this $I_n(t)$ histogram. σ_n is the summation of the σ_M and the oscilloscope noise (σ_0) according to $\sigma_M = \sqrt{{\sigma_n}^2 - {\sigma_0}^2}$. σ_M is a measure of the fluctuation in the multiplication factor (M) due to the statistical nature of the avalanche process [34].

The estimated σ_M for both types of RTSs for all diodes are shown in Fig. 16(c)-(d). σ_M remains almost constant with V_{EX}. A constant σ_M implies that the fluctuation in M is relatively constant with V_{EX}. This has been reported earlier that the noise becomes independent of M for large

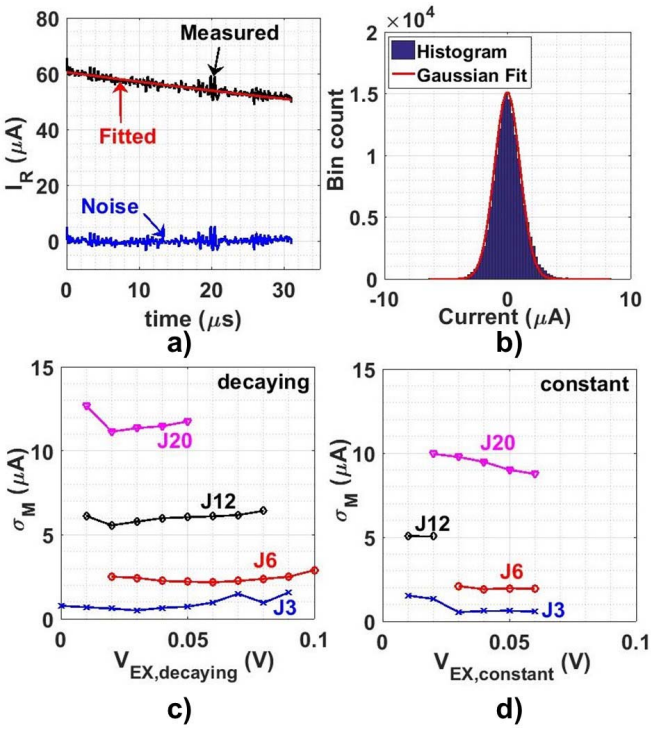

FIGURE 16. **a) Example procedure for estimating the noise transient $I_n(t)$. b) Example histogram and the fitted Gaussian of the obtained I_n of the "decaying" amplitude RTSs in J3 at $V_R = 13.87$ V. c) σ_M for the "decaying" amplitude RTSs. d) σ_M for the "constant" amplitude RTSs.**

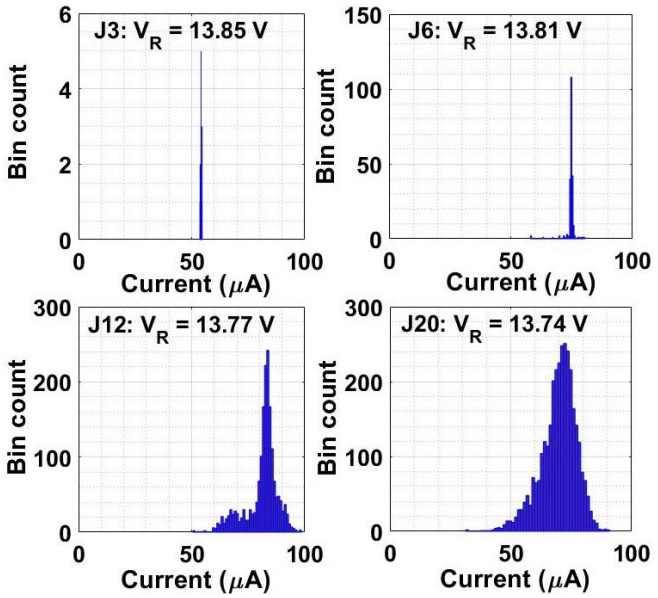

FIGURE 17. **Histogram of the "decaying" I_{peak} at specified bias points in all diodes. Y-axis scales are different for clarity. The wider distribution of I_{peak} in larger diodes can be attributed to random fluctuations at more number of defects.**

values of M [34], [35]. Further, noise decreased with increasing avalanche current if the defects would be stable and would not cause any RTS fluctuations [35]. In particular, the unstable defects increase the noise [35]. In our operating bias range, the increasing noise contributed by the unstable defects possibly counteract the decrease in noise induced by the increasing current and therefore a relatively constant σ_M is observed.

In addition, σ_M increases for larger diodes. This is because for a larger diode, the number of defects increases, resulting in noise originating from multiple RTS phenomena [26].

APPENDIX B
DISTRIBUTION OF PEAK CURRENT

We have assumed a mean I_{peak} in Section V. As discussed there, in large diodes, the avalanche most likely spreads to nearby defects by lateral transport of free carriers and emission of secondary photons. This effect can be observed from the I_{peak} histogram. An example of the histogram of the I_{peak} for "decaying" amplitude RTSs for all diodes at indicated bias settings are shown in Fig. 17. A wider distribution in I_{peak} for large diodes is obtained. This is likely due to the random fluctuations in the triggering of avalanche at different defects in larger diodes.

APPENDIX C
LIGHT EMISSION PROFILES

It is commonly known that during avalanche, Si p-n junctions emit visible light [7], [8], though with a low internal quantum efficiency ($\sim 10^{-5}$) [10]. The shallow junctions in our devices allow to observe the light emission from these devices using a visible wavelength camera.

Fig. 18(a) shows some micrographs of these diodes. Fig. 18(b) shows the light emission from these devices during the instability region captured using a Nikon D3100 camera with an integration time of 30 s. These emissions were observed at a relatively high V_R; at those V_R mostly "constant" amplitude type of RTSs were observed ($F \sim 1$). At lower V_R, the light emission intensity was too low to be detected by our camera. Further, for smaller diodes, the light emission appears to be uniform whereas for larger diodes (e.g., J20), the light emitting spots are aligned at the periphery. The light emission from localized spots imply that an RTS in avalanche diodes is a localized phenomenon.

Fig. 18(c) shows the normalized intensity profiles of the light emission. A non-uniform emission from the localized spots can be seen for the large diodes (e.g., J20). Fig. 18(d) shows the contour plots of the light emission and localized light emitting spots in large devices can be observed.

From Fig. 18(b) and the camera resolution, the area of the light emitting spots can be estimated. At the measured camera settings, one image pixel area (A_{pixel}) ~ 0.002 μm^2. From the intensity profiles (Fig. 18(c)), the number of pixels with an intensity higher than a threshold (N_{pixels}) was estimated. Then, the area of the light emitting spot was estimated as $A_{spot} = N_{pixels} \times A_{pixel}$. From A_{spot}, an effective d of the light emitting spot was estimated as $d = \sqrt{4A_{spot}/\pi}$; the

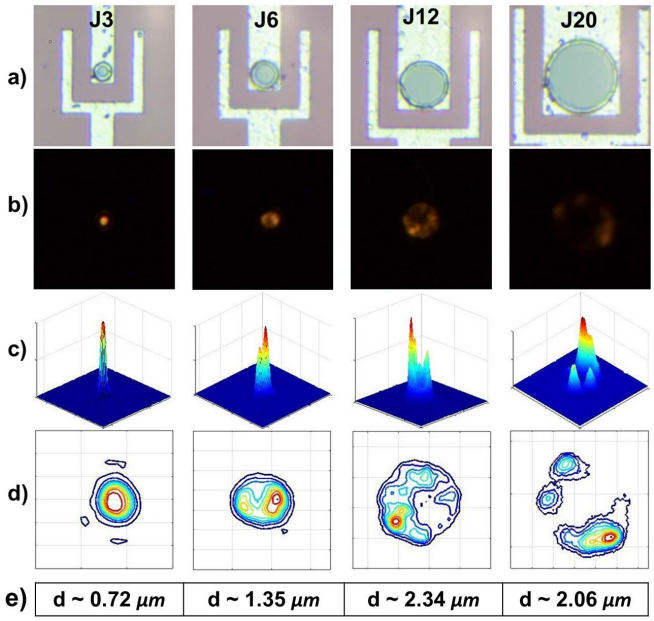

FIGURE 18. a) Device micrographs. b) Light emission captured using a Nikon D3100 Visible wavelength camera with an integration time of 30 s. c) Normalized intensity profiles, d) Normalized contour profiles of the light emission from these junctions. Note that (b) is to scale whereas for (c) and (d) the axis scales are different to enhance the clarity. e) Estimated *d* of the defects causing "constant" amplitude RTSs from the light emitting spots.

results are shown in Fig. 18(e). A close agreement with the estimated d in Fig. 14(c) was obtained. The d for J12 is larger than that for J20 as was also estimated in Fig. 14(c). The slight difference with the d estimated using the $I_{\text{peak}} - V_{\text{EX}}$ characteristics can be attributed to the low intensity of emission at some pixels that could not be measured by our camera.

ACKNOWLEDGMENT

The authors would like to acknowledge Dr. Lin Qi for fabricating these devices and Henk de Vries for help with the experiments. We also thank Dr. Jurriaan Schmitz for a critical review of the manuscript.

REFERENCES

[1] W. G. Oldham, R. R. Samuelson, and P. Antognetti, "Triggering phenomena in avalanche diodes," *IEEE Trans. Electron Devices*, vol. ED-19, no. 9, pp. 1056–1060, Sep. 1972, doi: 10.1109/T-ED.1972.17544.

[2] R. J. McIntyre, "On the avalanche initiation probability of avalanche diodes above the breakdown voltage," *IEEE Trans. Electron Devices*, vol. ED-20, no. 7, pp. 637–641, Jul. 1973, doi: 10.1109/T-ED.1973.17715.

[3] O. Marinov, M. J. Deen, and J. A. J. Tejada, "Theory of microplasma fluctuations and noise in silicon diode in avalanche breakdown," *J. Appl. Phys.*, vol. 101, no. 6, 2007, Art. no. 064515, doi: 10.1063/1.2654973.

[4] R. J. E. Hueting *et al.*, "An improved analytical model for carrier multiplication near breakdown in diodes," *IEEE Trans. Electron Devices*, vol. 64, no. 1, pp. 264–270, Jan. 2017, doi: 10.1109/TED.2016.2630083.

[5] B. Razavi, *Design of Integrated Circuits for Optical Communications*, New York, NY, USA: McGraw-Hill, 2003.

[6] E. Charbon, "Single-photon imaging in complementary metal oxide semiconductor processes," *Philosoph. Trans. Roy. Soc. A Math. Phys. Eng. Sci.*, vol. 372, Mar. 2014, Art. no. 20130100, doi: 10.1098/rsta.2013.0100.

[7] R. Newman, "Visible light from a silicon p-n junction," *Phys. Rev.*, vol. 100, no. 2, pp. 700–703, 1955, doi: 10.1103/PhysRev.100.700.

[8] L. W. Snyman *et al.*, "Optical sources, integrated optical detectors, and optical waveguides in standard silicon CMOS integrated circuitry," in *Proc. SPIE*, vol. 3953. San Jose, CA, USA, 2000, pp. 20–36, doi: 10.1117/12.379613.

[9] B. Huang *et al.*, "CMOS monolithic optoelectronic integrated circuit for on-chip optical interconnection," *Opt. Commun.*, vol. 284, nos. 16–17, pp. 3924–3927, 2011, doi: 10.1016/j.optcom.2011.04.028.

[10] S. Dutta, V. Agarwal, R. J. E. Hueting, J. Schmitz, and A. J. Annema, "Monolithic optical link in silicon-on-insulator CMOS technology," *Opt. Exp.*, vol. 25, no. 5, pp. 5440–5456, 2017, doi: 10.1364/OE.25.005440.

[11] K. G. McKay, "Avalanche breakdown in silicon," *Phys. Rev.*, vol. 94, no. 4, pp. 877–884, 1954, doi: 10.1103/PhysRev.94.877.

[12] D. J. Rose, "Microplasmas in silicon," *Phys. Rev.*, vol. 105, no. 2, pp. 413–418, 1957, doi: 10.1103/PhysRev.105.413.

[13] A. G. Chynoweth and K. G. Mckay, "Light emission and noise studies of individual microplasmas in silicon *p-n* junctions," *J. Appl. Phys.*, vol. 30, no. 11, pp. 1338–1348, 1961, doi: 10.1063/1.1735060.

[14] K. S. Champlin, "Microplasma fluctuations in silicon," *J. Appl. Phys.*, vol. 30, no. 7, pp. 1039–1050, 1959, doi: 10.1063/1.1776976.

[15] W. Shockley, "Problems related to p-n junctions in silicon," *Solid State Electron.*, vol. 2, no. 1, pp. 35–67, 1961, doi: 10.1016/0038-1101(61)90054-5.

[16] R. J. McIntyre, "Theory of Microplasma instability in silicon," *J. Appl. Phys.*, vol. 32, no. 6, pp. 983–995, 1961, doi: 10.1063/1.1736199.

[17] R. H. Haitz, "Model for the electrical behavior of a microplasma," *J. Appl. Phys.*, vol. 35, no. 5, pp. 1370–1376, 1964, doi: 10.1063/1.1713636.

[18] V. Agarwal *et al.*, "Random telegraph signal phenomena in avalanche mode diodes: Application to SPADs," in *Proc. 46th Eur. Solid State Device Res. Conf. (ESSDERC)*, Lausanne, Switzerland, 2016, pp. 264–267, doi: 10.1109/ESSDERC.2016.7599636.

[19] O. Marinov, M. J. Deen, V. Loukanov, and V. Velikov, "The low frequency noise in reverse biased rectifier diodes," *IEEE Trans. Electron Devices*, vol. 49, no. 1, pp. 184–187, Jan. 2002, doi: 10.1109/16.974768.

[20] P. G. Neudeck, W. Huang, and M. Dudley, "Breakdown degradation associated with elementary screw dislocations in 4H-SiC p^+n junction rectifiers," *Solid State Electron.*, vol. 42, no. 12, pp. 2157–2164, 1998, doi: 10.1016/S0038-1101(98)00211-1.

[21] L. K. Nanver *et al.*, "Applications of PureB and PureGaB ultrashallow junction technologies," in *Proc. IEEE 11th Int. Conf. Solid State Integr. Circuit Technol.*, 2012, pp. 1–4, doi: 10.1109/ICSICT.2012.6467697.

[22] L. Qi *et al.*, "UV-sensitive low dark-count PureB single-photon avalanche diode," *IEEE Trans. Electron Devices*, vol. 61, no. 11, pp. 3768–3774, Nov. 2014, doi: 10.1109/ICSENS.2013.6688603.

[23] L. K. Nanver *et al.*, "Robust UV/VUV/EUV PureB photodiode detector technology with high CMOS compatibility," *IEEE J. Sel. Topics Quantum Electron.*, vol. 20, no. 6, pp. 306–316, Nov./Dec. 2014, doi: 10.1109/JSTQE.2014.2319582.

[24] M. S. Tyagi, *Introduction to Semiconductor Materials and Devices*. New York, NY, USA: Wiley, 1991.

[25] D. A. Ramirez, M. M. Hayat, G. J. Rees, X. Jiang, and M. A. Itzler, "New perspective on passively quenched single photon avalanche diodes: Effect of feedback on impact ionization," *Opt. Exp.*, vol. 20, no. 2, pp. 1512–1529, 2012, doi: 10.1364/OE.20.001512.

[26] M. J. Kirton and M. J. Uren, "Noise in solid state microstructures: A new perspective on individual defects, interface states and low frequency (1/f) noise," *Adv. Phys.*, vol. 38, no. 4, pp. 367–468, 1989, doi: 10.1080/00018738900101122.

[27] S. M. Sze and W. Shockley, "Unit-cube expression for space-charge resistance," *Bell Syst. Tech. J.*, vol. 46, no. 5, pp. 837–842, 1967, doi: 10.1002/j.1538-7305.1967.tb01716.x.

[28] S. M. Sze and K. K. Ng, *Physics of Semiconductor Devices*. Hoboken, NJ, USA: Wiley, 2007.

[29] M. Schroter and A. Chakravorty, *Compact Hierarchical Bipolar Transistor Modeling With HICUM* (International Series on Advances in Solid State Electronics and Technology). Hackensack, NJ, USA: World Sci., 2010.

[30] C. R. Crowell and S. M. Sze, "Temperature dependence of avalanche multiplication in semiconductors," *Appl. Phys. Lett.*, vol. 9, no. 6, pp. 242–244, 1966, doi: 10.1063/1.1754731.
[31] C. Y. Chang, S. S. Chiu, and L. P. Hsu, "Temperature dependence of breakdown voltage in silicon abrupt p-n junctions," *IEEE Trans. Electron Devices*, vol. ED-18, no. 6, pp. 391–393, Jun. 1971, doi: 10.1109/T-ED.1971.17210.
[32] A. Spinelli and A. L. Lacaita, "Physics and numerical simulation of single photon avalanche diodes," *IEEE Trans. Electron Devices*, vol. 44, no. 11, pp. 1931–1943, Nov. 1997, doi: 10.1109/16.641363.
[33] T. L. Bergman, A. S. Lavine, F. P. Incropera, and D. P. DeWitt, *Fundamentals of Heat and Mass Transfer*. New York, NY, USA: Wiley, 2007.
[34] R. J. McIntyre, "Multiplication noise in uniform avalanche diodes," *IEEE Trans. Electron Devices*, vol. ED-13, no. 1, pp. 164–168, Jan. 1966, doi: 10.1109/T-ED.1966.15651.
[35] R. H. Haitz, "Noise of a self–sustaining avalanche discharge in silicon: Low–frequency noise studies," *J. Appl. Phys.*, vol. 38, no. 7, pp. 2935–2946, 1967, doi: 10.1063/1.1710027.

VISHAL AGARWAL received the bachelor's and master's degrees in electrical engineering from IIT Kanpur, India, in 2011. He is currently pursuing the Ph.D. degree with the Integrated Circuit Design Group, University of Twente, Enschede, The Netherlands.

From 2011 to 2014, he was with Intel Technology India Pvt., Ltd., Bengaluru, India.

ANNE-JOHAN ANNEMA received the M.Sc. degree in electrical engineering and the Ph.D. degree from the University of Twente, Enschede, The Netherlands, in 1990 and 1994, respectively. In 1995, he joined the Semiconductor Device Architecture Department, Philips Research, Eindhoven, The Netherlands, where he researched on a number of physics-electronics-related projects. In 1997, he joined the Mixed-Signal Circuits and Systems Department, Philips Research, where he researched on a number of electronics-physics-related projects ranging from low-power low-voltage circuits, fundamental limits on analog circuits in conjunction with process technologies, high-voltage in baseline CMOS to feasibility research of future CMOS processes for analog circuits.

Since 2000, he has been with the IC-Design Group, Department of Electrical Engineering, University of Twente, Enschede, The Netherlands, where he is an Associate Professor. His current research focus is on semiconductor physics, analog and mixed-signal electronics, RF power circuits, and technology/physics related circuit design. He is also a part-time consultant in industry and in 2001 he co-founded ChipDesignWorks.

SATADAL DUTTA (S'15) received the B.Tech. degree (Hons.) in electronics and electrical communication engineering and the M.Tech. degree in microelectronics and VLSI from IIT Kharagpur, Kharagpur, India, in 2013, and the Ph.D. degree from the MESA+ Institute for Nanotechnology, University of Twente, Enschede, The Netherlands, in 2017. His current research interests include semiconductor device physics, optics, and optoelectronics.

RAYMOND J. E. HUETING (S'94–M'98–SM'06) received the M.Sc. *(cum laude)* and Ph.D. degrees in electrical engineering from the Delft University of Technology, The Netherlands with the Ph.D. thesis dealt with the device physics of SiGe-based heterojunction bipolar transistors. In 1997, he joined Philips both in the Netherlands and Belgium, where he researched on device physics of power MOSFET's and SiGe-based heterojunction devices. In 2005, he joined the Integrated Devices & Systems (formerly, Semiconductor Components) Group, MESA+ Institute for Nanotechnology, University of Twente, the Netherlands, where he has been involved in the field of semiconductor device physics and modeling.

He has authored and co-authored over 80 papers and 35 U.S. patents. He participates and participated in the technical programme committee of the ESSDERC and the ISPSD conference, respectively.

LIS K. NANVER (LM'80) received the master's degree in physics from the University of Aarhus, Denmark, in 1979, and the docteur ingenieur degree in physics applied to telecommunications from the Ecole Nationale Supérieure des Télécommunications, Paris, France, in 1982, and the Ph.D. degree in electrical engineering from the Delft University of Technology, The Netherlands, in 1987.

Since 1987, she has been a Researcher with the Delft University of Technology, where she has been a Professor since 2001. Since 2015, she has also been a Guest Professor with the University of Twente, Enschede, The Netherlands, and Aalborg University, Aalborg, Denmark. Her main research interests are new devices and integration processes, mainly for RF, microwave, or smart sensor applications. She has pioneered several new technologies such as substrate transfer for true two-sided contacting, and ultrashallow junction diodes using laser annealing/solid-phase epitaxy. Her research on new pure-dopant CVD processes for creating extremely shallow diodes (PureB for Si and PureGaB for Ge devices) has resulted in several leading-edge applications such as high-linearity silicon-on-glass varactor diodes, Si photodiode detectors for low penetration-depth beams, and low-leakage Ge-on-Si photodiodes.

Prof. Nanver was a recipient of several prizes, including the 2010 IEDM Roger Haken Award. She is an Associate Editor of the IEEE ELECTRON DEVICE LETTERS and has served on the committees of BCTM and ESSDERC.

BRAM NAUTA (S'89–M'91–SM'03–F'08) was born in Hengelo, The Netherlands, in 1964. He received the M.Sc. degree *(cum laude)* in electrical engineering and the Ph.D. degree in analog CMOS filters for very high frequencies from the University of Twente, Enschede, The Netherlands, in 1987 and 1991, respectively.

In 1991, he joined the Mixed-Signal Circuits and Systems Department, Philips Research, Eindhoven, The Netherlands. In 1998, he returned to the University of Twente, where he is currently a Distinguished Professor, heading the IC Design Group. Since 2016, he has been serving as the Chair with the Electrical Engineering Department, University of Twente. His current research interest include high-speed analog CMOS circuits, software defined radio, cognitive radio, and beamforming.

Dr. Nauta was a co-recipient of the ISSCC 2002 and 2009 Van Vessem Outstanding Paper Award, the Simon Stevin Meester Award (500.000 €) in 2014, and the Largest Dutch National Prize for achievements in technical sciences. He served as the Editor-in-Chief from 2007 to 2010 for the IEEE JOURNAL OF SOLID-STATE CIRCUITS (JSSC), and was the 2013 Program Chair of the IEEE International Solid-State Circuits Conference. He is the President of the IEEE Solid-State Circuits Society from 2018 to 2019. Also, he served as an Associate Editor for the IEEE TRANSACTIONS ON CIRCUITS AND SYSTEMS—PART II: EXPRESS BRIEFS from 1997 to 1999 and for JSSC from 2001 to 2006. He was on the Technical Program Committee of the Symposium on VLSI Circuits from 2009 to 2013. He is on the Steering Committee and Program Committee of the European Solid-State Circuit Conference. He has served as a Distinguished Lecturer for the IEEE. He is a member of the Royal Netherlands Academy of Arts and Sciences.